Original Paper

Eletrônica de Potência
Open Journal of Power Electronics

Received August 28, 2025; Received in revised form December 02, 2026 and January 16, 2026; Accepted January 29, 2026; Date of publication March 09, 2026.
The review of this paper was arranged by Associate Editor Allan F. Cupertino and Editor-in-Chief Heverton A. Pereira.
Digital Object Identifier http://doi.org/10.18618/REP.e202615

Notch-Filter-Based Control Strategy to Extend Stability Limits of LCL-Filtered Grid-Connected Inverters

James N. Silva[1,*], **Filipe A. da C. Bahia**[1], **Andre P. N. Tahim**[1], **Darlan A. Fernandes**[2], **Fabiano F. Costa**[1]

[1]Federal University of Bahia, Department of Electrical and Computer Engineering, Salvador – BA, Brazil.
[2]Federal University of Paraíba, Department of Electrical Engineering, João Pessoa – PB, Brazil.

e-mail: james.silva@ufba.br*; filipe.bahia@ufba.br; atahim@ufba.br; darlan@cear.ufpb.br; fabiano.costa@ufba.br.
*Corresponding author.

ABSTRACT The stable connection of energy sources to the grid via LCL-filtered inverters is often constrained by delays introduced by digital implementation and DPWM modulation. This paper proposes a novel notch-filter-based compensation strategy that explicitly mitigates such delays, extending the stability region of the current control system by increasing the critical frequency. In addition, a systematic methodology is introduced for tuning the active damping gain, demonstrating its direct influence on phase margin and robustness – an aspect not systematically addressed in previous studies. Unlike approaches based on auto-tuning or real-time resonance estimation, the proposed method imposes no additional computational burden while significantly expanding the stability limits. Analytical studies, frequency-domain analysis, and experimental validation using a hardware-in-the-loop (HIL) platform confirm that the proposed strategy extends the stable operating region, improves dynamic performance, and reduces harmonic distortion, representing a distinctive contribution to the control of LCL-filtered grid-connected inverters.

KEYWORDS Grid-connected inverter, LCL filter, Nyquist stability criterion, Active damping, Hardware-in-the-loop.

I. INTRODUCTION

LCL filters are widely adopted in grid-connected converters due to their superior harmonic attenuation and smaller size compared to purely inductive filters [1], [2]. However, the resonance peak inherent to the LCL filter poses critical stability challenges, largely resulting from delays associated with the digital implementation of the control systems and the inverter's DPWM [3], [4].

It is known that the so-called critical frequency, f_c, delimits regions of stability and instability for the location of the filter's resonance peak [5]. This critical frequency, in turn, is associated with the time delay originating from the digital implementation mentioned earlier. When the control variable is the grid-injected current, which is the focus of this work, the stability region is bounded above the critical frequency. In practice, since resonance peaks of typical LCL filters occur in the lower frequency range, this constraint can severely limit both the design and robustness of the control system, particularly in weak grids. A common solution to this problem is the addition of an active damping loop based on capacitor-current feedback [6]. This active damping shifts the stability region below f_c, enabling its expansion through time-delay reduction techniques, thereby enhancing the system's dynamic performance and increasing the control bandwidth [7], [8]. With this technique, the system becomes stable for resonance frequencies between 0 and f_c, and unstable between f_c and $f_s/2$, where f_s is the sampling frequency and $f_c = f_s/6$ is the critical frequency [3]. Nevertheless, merely adding an active damping loop does not guarantee stability: as verified in this work, the stability condition in the low-frequency region depends on the gain defined for this loop [9], [10]. Improper tuning of the damping gain, K_{ad}, may even reduce phase margins and compromise robustness. Despite its importance, the effect of K_{ad} on the system's stability margins has not been systematically addressed in the literature, where it is usually treated only as a stabilizing parameter.

Several alternative approaches have been investigated, including auto-tuning and resonance-frequency tracking techniques [11], which dynamically adjust notch filters to match the LCL filter's resonance. Although innovative, these approaches impose high computational costs and additional delays, limiting their applicability in real-time control. To overcome these limitations, this paper proposes a novel notch-filter-based compensator specifically designed to mitigate time delays. Unlike the aforementioned approaches, the proposed compensator provides a phase-lead effect that counteracts delay resulting from digital implementation of the control systems and the inverter's DPWM, shifting the critical frequency from $f_s/6$ to approximately $f_s/3$. This

extends the stable operating region and enhances the robustness of the control system to variations in grid and filter parameters. Furthermore, a new methodology for analyzing and tuning the active damping gain (K_{ad}) is presented. By explicitly relating K_{ad} to the system's phase margin, this work provides clear guidelines for its optimal selection, filling a notable gap in the literature.

The contributions of this paper can be summarized as follows:

1) A compensator that explicitly counteracts delays arising from the digital implementation of the control system and inverter modulation, without adding computational burden, significantly expanding the stable operating region of LCL-filtered inverters.
2) A systematic methodology for tuning the active damping gain (K_{ad}), with an explicit analysis of its influence on phase margin and robustness.
3) Experimental validation using a hardware-in-the-loop (HIL) platform, confirming that the proposed approach improves stability margins, reduces harmonic distortion, and enhances robustness, ensuring stable operation under varying resonance conditions.

The remainder of this paper is organized as follows. Section II establishes the system model and time delay representation. Section III analyzes the system's stability regions and introduces a systematic methodology for tuning the active damping gain (K_{ad}). Section IV presents the core contribution: the proposed notch-filter compensator for stability margin expansion. Section V presents experimental validation using a hardware-in-the-loop (HIL) platform. Finally, Section VI concludes the paper by summarizing the key findings and contributions.

II. SYSTEM MODELING

Fig. 1 shows the typical general structure of a Voltage Source Inverter (VSI) connected to the grid through an LCL filter, which consists of an inverter-side inductor, L_1, a grid-side inductor, L_2, and a filter capacitor, C. The purpose of this LCL filter is to attenuate harmonic distortions, especially those arising from switching. From a control perspective, the primary objective for this inverter topology is to act on the filter output current, i_2, and thereby control the active power injected into the grid. In this regard, the system must be robust enough to remain stable over the widest possible range of variations in the filter's resonance frequency.

Considering that the inverter's control system will be implemented in a Digital Signal Processor (DSP), it is necessary to model the system in the discrete-time domain. In this context, the discrete transfer functions that model the inverter are represented in the block diagrams of Fig. 2. For the analysis of the control system shown in this figure, three discrete-time transfer functions associated with the LCL filter must be obtained, namely: $G_{i2}(z)$, $G_{ic}(z)$, and $G_o(z)$. As a preliminary step to discretization, the Laplace domain expressions representing the equivalent continuous models of these functions are used. The functions $G_{i2}(s)$ and $G_{ic}(s)$, which describe the LCL filter dynamics, are given by:

$$G_{i2}(s) = \frac{i_2(s)}{V_o(s)} = \frac{1}{sL_1}\frac{\omega_o^2}{s^2 + \omega_r^2} \tag{1}$$

and

$$G_{ic}(s) = \frac{i_c(s)}{V_o(s)} = \frac{1}{sL_1}\frac{s^2}{s^2 + \omega_r^2}, \tag{2}$$

where

$$\omega_r = \sqrt{\frac{L_1 + L_2}{L_1 L_2 C}} \tag{3}$$

and

$$\omega_0 = \sqrt{\frac{1}{L_2 C}}. \tag{4}$$

The third transfer function, $G_o(s)$, is obtained in the Laplace domain through the ratio between $G_{i2}(s)$ and $G_{ic}(s)$, resulting in:

$$G_o(s) = \frac{G_{i2}(s)}{G_{ic}(s)} = \frac{\omega_0^2}{s^2}. \tag{5}$$

The transfer functions $G_{i2}(s)$ and $G_{ic}(s)$ given above can be discretized using ordinary *Z-transforms*. However, it is necessary to consider the typical time delay of the DPWM, which impacts these transfer functions. This is because the DPWM is part of the control loop as an output stage, responsible for controlling the states of the inverter switches, as can be seen in Fig. 1. One way to model this time delay caused by the DPWM is through a Zero Order Hold (ZOH), as detailed below [12].

Initially, the DPWM module receives at its input the discrete signal from the control algorithm. In response, it generates a continuous-time signal through pulse width modulation. Although the waveform generated by the DPWM differs from that produced by a Zero Order Hold (ZOH), the average effect of this modulation on the plant is equivalent to that of a ZOH. This equivalence is valid because the DPWM applies a constant control value to the plant throughout each modulation period with an average equal to the digital output provided by the controller — a behavior analogous to that of a ZOH, which holds the sample value until the next update. Furthermore, as demonstrated in [3], the ZOH naturally imposes an average effective delay of half a sampling period ($T_s/2$) on the system which resembles the delay observed between the instant of control calculation and its effective application to the plant via DPWM. Therefore, the ZOH is widely used to model the behavior of the DPWM in digital control systems [12]. For illustration purposes, an example of this typical ZOH delay can be seen in Fig. 3, where it is possible to note that the reconstructed output signal, represented by the fundamental component of the sampled

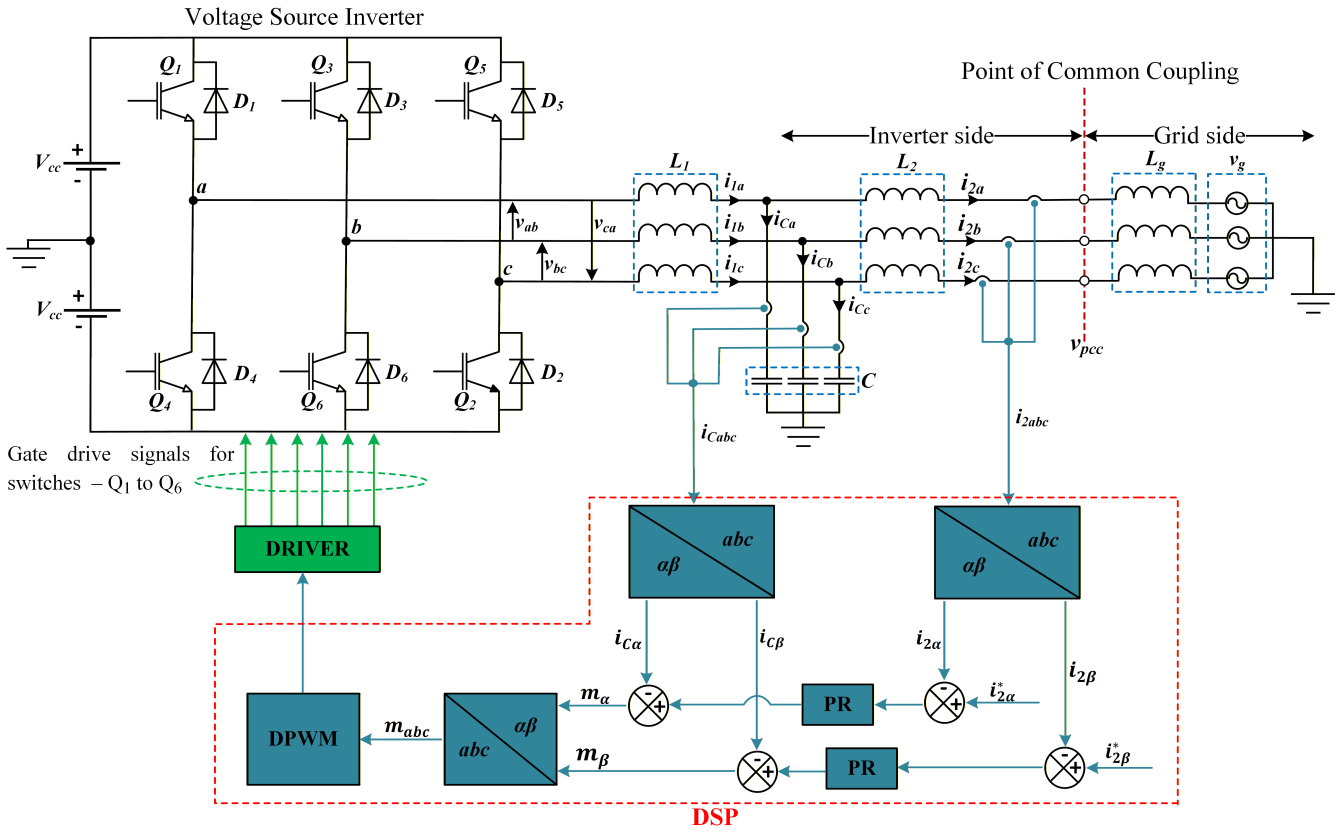

FIGURE 1. Control structure of a three-phase Voltage Source Inverter (VSI) connected to the grid through an LCL filter. The system includes active damping via proportional capacitor-current feedback.

signal (in blue in the figure), exhibits an average delay of half a sampling period with respect to the input signal.

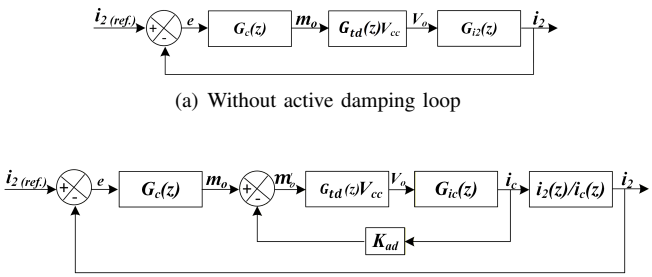

(a) Without active damping loop

(b) With active damping

FIGURE 2. Equivalent block diagrams for inverter current control.

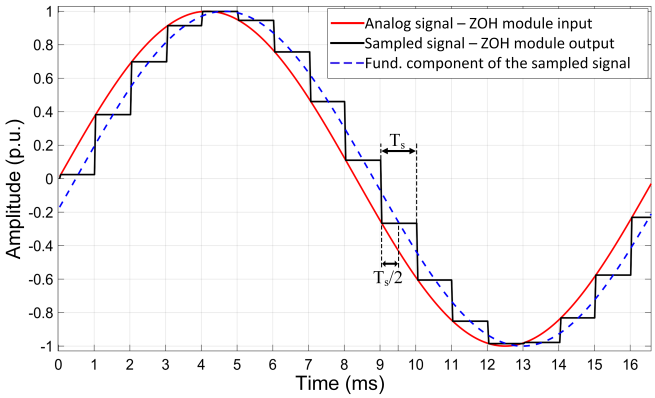

FIGURE 3. Time delay introduced by a ZOH module with $T_s = 1$ ms. The input is a 60 Hz analog signal, and the output is a sampled signal exhibiting an average delay of $T_s/2$ ms with respect to the input.

Revisiting the discretization of the previously mentioned transfer functions $G_{i2}(s)$ and $G_{ic}(s)$, the ZOH model is now incorporated. This model is widely used in the literature to introduce the effects of the time delay inherent to the DPWM, as previously discussed. For this purpose, the ZOH transfer function used is given by

$$H(s) = \frac{1 - e^{-sT_s}}{s}, \tag{6}$$

where T_s represents the sampling period, adopted as T_s=1/f_s. The objective of including this transfer function in the discretization process of $G_{i2}(s)$ and $G_{ic}(s)$ is to obtain discrete versions of these transfer functions that inherently incorporate the effects of the average delay introduced by the DPWM, which is equivalent to $T_s/2$.

The transfer function (6) accounts for the equivalent delay of $T_s/2$ and the frequency-dependent attenuation intro-

duced by $\mathrm{sinc}(\omega T_s/2\pi)$. Although this attenuation increases with frequency, it remains close to 0 dB throughout the control bandwidth—typically below 10% of the Nyquist frequency—and can therefore be neglected. Consequently, the ZOH is approximated as a pure delay of $T_s/2$, a standard assumption in digital control analysis. Therefore, the resulting discrete model will more accurately reflect the actual dynamics of the implemented digital system. Given this, the discretization of $G_{i2}(s)$ and $G_{ic}(s)$ can then be performed by applying ordinary *Z-transforms*, resulting in

$$G_{i2}(z) = Z\Big\{H(s)G_{i2}(s)\Big\} = Z\left\{\frac{1-e^{-sT_s}}{s}G_{i2}(s)\right\}, \quad (7)$$

and

$$G_{ic}(z) = Z\Big\{H(s)G_{ic}(s)\Big\} = Z\left\{\frac{1-e^{-sT_s}}{s}G_{ic}(s)\right\}. \quad (8)$$

By definition, $Z\Big\{1-e^{-sT_s}\Big\} = 1-z^{-1}$, such that $G_{i2}(z)$ and $G_{ic}(z)$ can be rewritten as

$$G_{i2}(z) = (1-z^{-1})Z\left\{\frac{G_{i2}(s)}{s}\right\}, \quad (9)$$

$$G_{ic}(z) = (1-z^{-1})Z\left\{\frac{G_{ic}(s)}{s}\right\}. \quad (10)$$

Finally, the discretization yields the following transfer functions, where $L = L_1 + L_2$.

$$G_{i2}(z) = \frac{T_s}{L(z-1)} - \frac{sin(\omega_r T_s)}{\omega_r L}\frac{z-1}{z^2 - 2zcos(\omega_r T_s) + 1} \quad (11)$$

$$G_{ic}(z) = \frac{sin(\omega_r T_s)}{\omega_r L_1}\frac{z-1}{z^2 \ - \ 2zcos(\omega_r T_s) + 1}. \quad (12)$$

When discretizing the transfer function $G_o(s)$, in turn, it is necessary to ensure that no additional time delay is introduced into the system. This is because the aforementioned transfer function derives from $G_{i2}(s)$ and $G_{ic}(s)$, whose respective discretizations performed previously already incorporate the appropriate time delay. In this regard, to ensure that no additional delay is inserted into the system, the *impulse invariance criterion* is applied to perform the transformation from the s-domain to the z-domain [13]. The purpose of this criterion is to ensure the equivalence of continuous and discrete systems, so that both have the same output, $y(t)$, if fed with the same input, $x(t)$. Based on these considerations, the discretization of $G_o(s)$ results in

$$G_o(z) = \frac{\omega_0^2 T^2 z}{(z-1)^2}. \quad (13)$$

While the delay arising from DPWM modulation (equivalent to $0.5T_s$) is already incorporated into the modeling of $G_{i2}(s)$ and $G_{ic}(s)$ via ZOH, as previously discussed, it is also essential to consider the computational delays inherent in the digital implementation of control algorithms. This arises because the controller's response at any given instant is computed using input signals sampled at a preceding instant. As a result, the control output consistently exhibits an average delay equivalent to one sampling period (T_s) relative to the input. This inherent delay can be effectively modeled as a pure time delay, expressed exponentially as

$$G_{td}(s) = e^{-T_s s}. \quad (14)$$

Thus, the total delay affecting the control loop is $1.5T_s$. This delay is the sum of $0.5T_s$ from DPWM modulation (already modeled via ZOH) and $1T_s$ from the computational delay modeled by

$$G_{td}(z) = z^{-1}. \quad (15)$$

The transfer functions $G_{i2}(z)$, $G_{ic}(z)$, and $G_{td}(z)$ are depicted in the block diagram of Fig. 2. This figure presents two configurations: Fig. II illustrates the system without active damping, while Fig. II includes active damping implemented through feedback of the capacitor current from the LCL filter. The current controller, denoted by the block $G_c(z)$, is of the Proportional-Resonant (PR) type, tuned to the grid fundamental frequency. This controller is widely used in such applications to eliminate steady-state error in current reference tracking. The continuous-time transfer function of the PR controller is given below as $G_c(s)$. In this expression, K_p represents the proportional gain, K_i the resonant gain, and ω_{res} the resonant frequency, which is set equal to the grid fundamental frequency in this case.

$$G_c(s) = K_p + K_i\frac{s}{s^2 + \omega_{res}^2}. \quad (16)$$

The transformation of $G_c(s)$ from the continuous-time domain to the discrete-time domain requires a more specific approach. This is due to the high sensitivity of PR controllers to discretization methods, given their narrow bandwidth and infinite gain at the resonant frequency. Such sensitivity can lead to significant performance degradation, even as a result of small shifts in the resonant poles, potentially causing the controller to behave as a purely proportional one.

To mitigate this performance loss, a commonly used discretization technique is the bilinear transform with prewarping, as it accurately preserves the controller's frequency response [14]. Using this method, the transfer function of the resonant controller can be expressed as

$$G_c(z) = K_p + K_i\frac{\sin(\omega_{res}T_s)}{2\omega_{res}}\frac{z^2-1}{(z^2 - 2z\cos(\omega_{res}T_s) + 1)}. \quad (17)$$

These transfer functions can be combined to obtain the open-loop expressions of the controllers shown in Fig. 2, for the purpose of applying frequency response and root locus techniques to the analysis of the systems. For the control

system without active damping, depicted in Fig. II, the open-loop transfer function can be expressed as

$$G_{ol}(z) = \frac{i_2(z)}{e(z)} = G_c(z)G_{td}(z)V_{cc}G_{i2}(z), \qquad (18)$$

where $e(z)$ represents the current error. In turn, for the system with active damping shown in Fig. II, it is first necessary to derive the closed-loop expression of the internal feedback loop associated with the capacitor current, that is,

$$G_{int}(z) = \frac{i_c(z)}{m_o(z)} = \frac{G_{td}(z)V_{cc}G_{i_c}(z)}{1 + K_{ad}G_{td}(z)V_{cc}G_{i_c}(z)}. \qquad (19)$$

The active damping action is implemented through capacitor current feedback with gain K_{ad}, forming an internal feedback loop whose purpose is to reshape the plant dynamics and suppress the LCL resonance. By closing this internal loop, an equivalent damped plant is obtained. Based on this equivalent representation, the open-loop transfer function of the external current control loop is derived by opening the loop at the output of the current controller.

By combining (19) with (11), (8), and (17), the open-loop transfer function of the system with active damping, as shown in Fig. II, can be obtained. For simplification, the resonant term in (17) can be omitted, since its influence is only significant near the resonant frequency ω_{res}, whereas the frequency range of interest — associated with the LCL filter resonance — is considerably higher than ω_{res}. Thus, $G_c(z)$ is reduced to the proportional constant K_p, as discussed in [15], and the open-loop transfer function of the system with active damping can be expressed as follows:

$$G_{ol}^{ad}(z) = G_c(z)\frac{i_c(z)}{m_o(z)}\frac{i_2(z)}{i_c(z)}, \qquad (20)$$

which is equivalent to

$$G_{ol}^{ad}(z) = \frac{K_pV_{cc}G_{td}(z)G_{i_c}(z)G_o(z)}{1 + K_{ad}V_{cc}G_{td}(z)G_{i_c}(z)}, \qquad (21)$$

and is used for open-loop frequency-domain stability analysis. Although the active damping gain K_{ad} operates in a feedback path, Eq. 21 represents an open-loop transfer function with respect to the current controller, after closing the active damping loop.

III. STABILITY ANALYSIS OF THE SYSTEM WITH AND WITHOUT ACTIVE DAMPING

The Bode plots presented in Fig. 4 and Fig. 5 illustrate the stability regions for the control systems without and with active damping, respectively. These plots were produced from the corresponding open-loop transfer functions, $G_{ol}(z)$ and $G_{ol}^{ad}(z)$, using the parameters listed in Table 1. The values $K_{ad} = 0.0015$ and $K_p = 0.0012$ were used in the plots, and their selection is justified in Subsections III-A and III-B. The LCL filter components (L_1, L_2, and C) were designed following methodologies proposed in the literature, notably in [16] and [17]. Additionally, as recommended in [16],the resonance frequency of the LCL filter was placed within the range between ten times the grid frequency (600 Hz) and half the switching frequency (5 kHz). This practice aims to mitigate the risk of instability and performance issues caused by resonance with low-order harmonics from the grid or high-order harmonics generated by the inverter switching process.

TABLE 1. Inverter Parameters

Parameters	Values
L_1	6.0 mH
L_2	1.8 mH
f_s	10.0 kHz
f_{sw}	5.0 kHz
f_c	1.67 kHz
V_{cc}	400.0 V
P	4.0 kW
Resonance Frequencies	
f_{r1}	1.34 kHz, $C = 9.50\ \mu$F
f_{r2}	1.67 kHz, $C = 6.08\ \mu$F
f_{r3}	2.00 kHz, $C = 4.22\ \mu$F
f_{r4}	2.40 kHz, $C = 2.93\ \mu$F

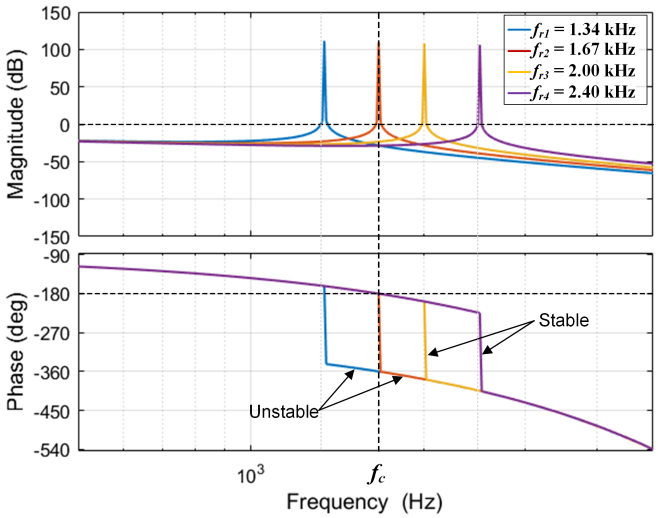

FIGURE 4. Bode plot of the current control system without active damping, with $K_p = 0.0012$.

From the frequency response of the undamped system shown in Fig. 4, it can be observed that for resonance frequencies below f_c, the phase crosses the -180° axis with a magnitude greater than 0 dB, indicating instability according to the Nyquist criterion. Conversely, for resonance frequencies above f_c, this crossing does not occur, and the system remains stable. When the active damping loop is introduced into the system, as illustrated in Fig. II, the previous scenario is reversed, such that the region below f_c becomes stable, as shown in Fig. 5. Furthermore, it is evident that instability occurs in both scenarios when the

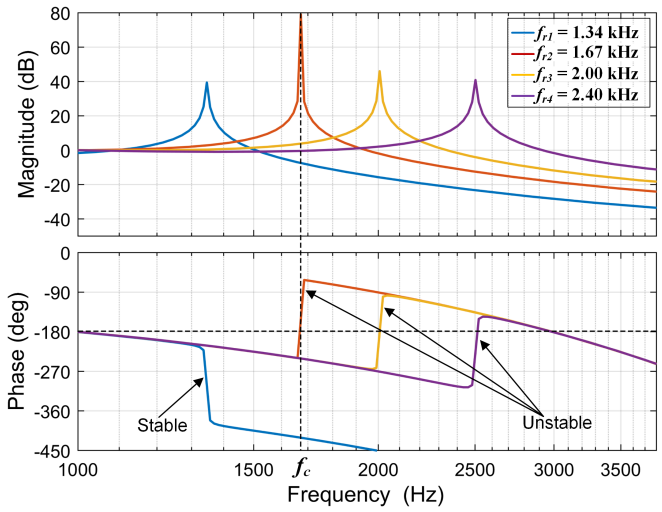

FIGURE 5. Bode plot of the current control system with active damping. In this plot, $K_p = 0.0012$, and $K_{ad} = 0.0015$.

resonance frequency f_{r2} coincides with f_c. At this point, both the damped and undamped systems are unstable.

The Bode plots presented in Fig. 4 and Fig. 5 demonstrate that the critical frequency, f_c, divides the regions of stability and instability at the point where the phase of the open-loop transfer function's frequency response reaches -180°. As shown in [3] and confirmed in this work, this occurs when $f_c = f_s/6$. If the LCL filter's resonance frequency is above this critical frequency, a control system without active damping may remain stable. However, if the filter's resonance frequency is below the critical frequency — which is the condition of interest in this article — the system's stability can only be ensured through an active damping loop with an appropriate gain.

A. ACTIVE DAMPING LOOP GAIN CONSTRAINTS

The limits for the active damping loop gain, K_{ad}, can be determined from the root locus of the closed-loop system, which indicates the pole locations as a function of K_{ad}. To this end, the characteristic equation of the system, i.e., $1 + G_{ol}^{ad}(z) = 0$, is used. This equation is developed below and presented as expression (22).

$$1 + K_{ad}V_{cc}G_{td}(z)G_{i_c}(z) + K_pV_{cc}G_{td}(z)G_{i_c}(z)G_o(z) = 0. \tag{22}$$

The authors in [6] rationalized that the proportional and damping gains, K_p and K_{ad}, are the main parameters governing the stability and dynamic performance of the control system. Through extensive numerical simulations, they evaluated the control behavior for different gain ratios and demonstrated that the condition $K_{ad} \geq K_p$ is required to ensure stability. The same fundamental reasoning is adopted in this paper. However, instead of relying only on numerical tuning, this work derives explicit analytical relationships between K_{ad} and K_p, which lead to a systematic design procedure for selecting K_{ad} rather than heuristic adjustment. Accordingly, (22) is rewritten by defining $K_p = nK_{ad}$, yielding

$$1 + K_{ad}[V_{cc}G_{td}(z)G_{i_c}(z) + nV_{cc}G_{td}(z)G_{i_c}(z)G_o(z) = 0. \tag{23}$$

Moreover, this analytical formulation provides the basis for the design of the proposed notch-based compensator, which is explicitly introduced to counteract the phase degradation caused by aforementioned delays. As a result, the critical frequency of the current control loop is shifted to higher values. While in [6] the critical frequency increases from approximately 1.67 kHz to 2.38 kHz, the methodology proposed in this work further extends it from 1.67 kHz to about 2.8 kHz, thereby enlarging the stable operating region of the system, as will be analytically and experimentally demonstrated in this article.

Using (23), the root locus diagram shown in Fig. 6 was obtained in order to determine the limits of K_{ad}. The parameters $n = 0.8$ and $f_r = 1.34$ kHz were adopted to ensure that $K_{ad} \geq K_p$ and $f_r < f_c$, respectively. In this figure, it can be observed that the resonant poles shift as K_{ad} increases. When the gain is between $K_{\text{ad(min)}}$ and $K_{\text{ad(max)}}$, the poles remain within the unit circle. Therefore, to ensure system stability, the gain K_{ad} must remain within the range defined by $K_{\text{ad(min)}}$ and $K_{\text{ad(max)}}$.

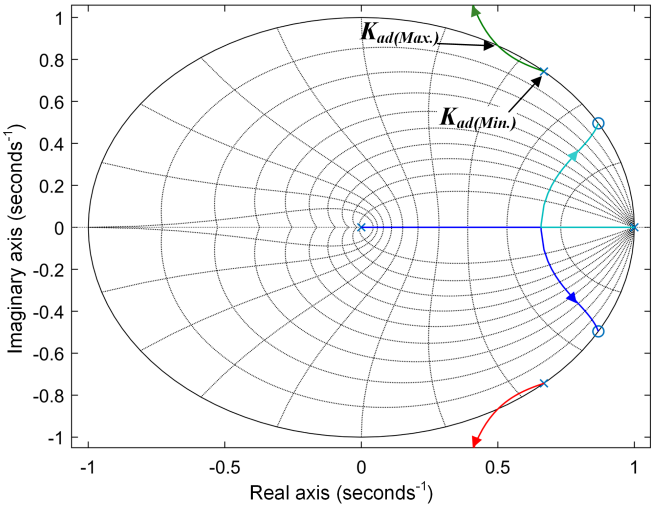

FIGURE 6. Root locus for the damped system considering $K_{ad} > K_p$ and $f_r < f_c$. The values of K_{ad} range from $K_{\text{ad(min)}} = 0.0015$ to $K_{\text{ad(max)}} = 0.090$.

By once again adopting (23), but now considering $f_r > f_c$, the root locus diagram shown in Fig. 7 was obtained. This diagram demonstrates that, even when $K_{ad} > K_p$, if the resonance frequency exceeds the critical frequency, the resonant poles follow trajectories outside the unit circle regardless of the value of K_{ad}. This confirms the instability condition of the actively damped system when the resonance frequencies are equal to or greater than f_c. The same instability condition

is also evident in the Bode plot shown in Fig. 5. On the other hand, as expected, the active damping effect is lost when $n > 1$, that is, when $K_{ad} < K_p$. In this case, resonant poles associated with frequencies above f_c become stable, as illustrated by the root locus diagram in Fig. 8. In other words, resonant poles associated with frequencies below f_c always follow paths outside the unit circle and are therefore unstable, while those associated with frequencies above f_c follow paths that pass through the interior of the unit circle. This behavior indicates a stability condition for resonance frequencies above f_c (f_{r3}, f_{r4}) and instability for those below f_c (f_{r1}), in agreement with the Bode plots of the undamped system shown in Fig. 4.

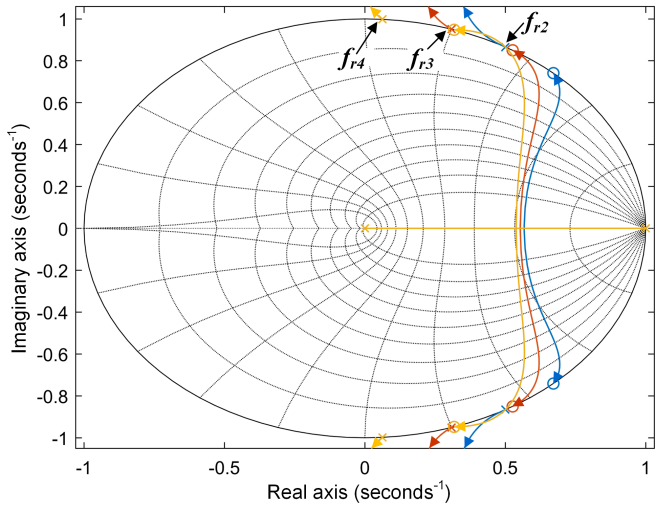

FIGURE 7. Root locus of the damped system with $K_{ad} > K_p$ and resonance frequencies higher than f_c.

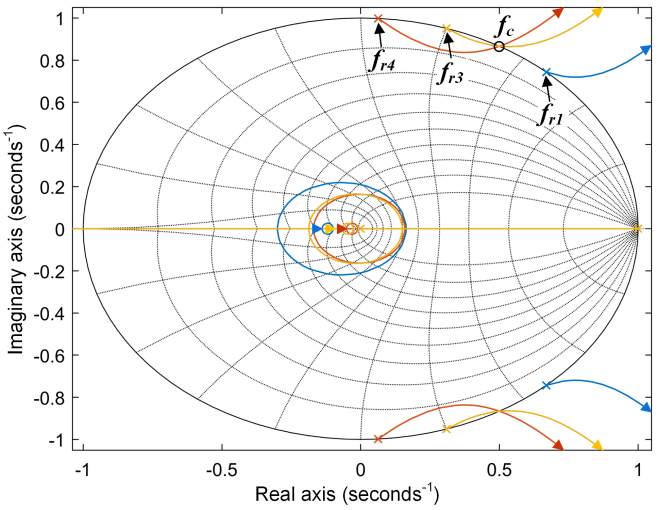

FIGURE 8. Root locus of the damped system with $K_{ad} < K_p$. The system remains stable for frequencies greater than f_c (f_{r3}, f_{r4}), and unstable for frequencies less than f_c (f_{r1}).

B. EFFECT OF K_{ad} ON SYSTEM PHASE MARGIN

The upper and lower limits for the active damping gain defined above, $K_{\text{ad(Max)}}$ and $K_{\text{ad(Min)}}$, ensure that the resonant poles remain within the unit circle. However, one of the contributions of this work is the verification that values of K_{ad} closer to $K_{\text{ad(Max)}}$ shift the resonant poles' frequency toward the critical frequency, f_c, which compromises the system's stability margin. This effect is evident in the Bode plot shown in Fig. 9, where increasing K_{ad} not only shifts the resonance peak toward f_c but also reduces the phase margin of the frequency response, thereby worsening the stability condition. This type of analysis, which is not found in the existing literature, demonstrates that the system can become unstable even when the LCL filter's resonance frequency f_r is lower than f_c, due to the resonance peak of the frequency response moving close to or beyond f_c as a result of increasing K_{ad}. In this context, the value of K_{ad} that optimizes the system's stability margins is $K_{ad} = K_{\text{ad(Min)}} = 0.0015$. This value was determined from the root locus diagram presented in Fig. 6, obtained using Matlab and adopted in this work. As shown in Fig. 9, this value yields the highest phase margin among the analyzed cases.

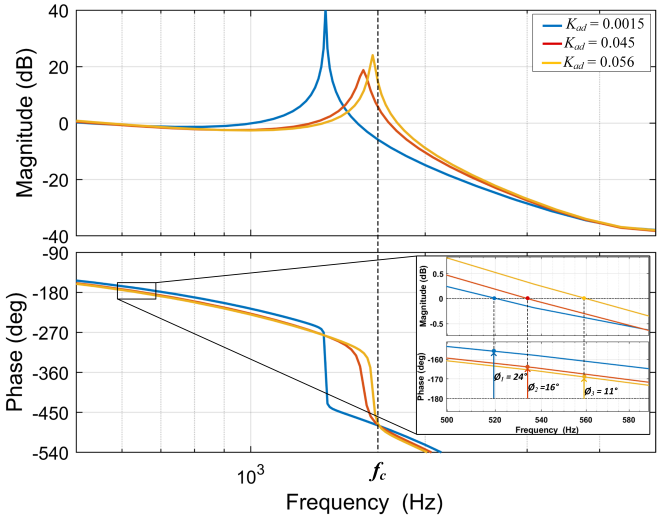

FIGURE 9. Bode plot of the damped system with varying K_{ad}. The LCL filter employed exhibits a resonant frequency of $f_r = 1.34\ kHz$. A shift of the resonance peak toward higher frequencies is observed, accompanied by a reduction in the phase margin due to the increase in K_{ad}.

IV. EXPANSION OF THE STABLE REGION OF THE DAMPED SYSTEM THROUGH NOTCH-BASED DELAY COMPENSATION

The analysis developed in the previous section demonstrates that the stability condition for systems with a resonance frequency below f_c is ensured by an internal feedback loop with a gain satisfying $K_{ad} \geq K_p$. In addition, the maximum and minimum limits for this gain have been determined.

Regarding the origin of the critical frequency that separates the stable and unstable regions of the control system,

it has been discussed in the previous sections that this frequency is directly related to the time delay introduced by the implementation of digital control and DPWM. This time delay manifests itself as a phase lag in the open-loop frequency response, directly affecting the system's stability margin. To mitigate this effect and extend the stability limits, it is necessary to shift the critical frequency to values higher than $f_s/6$, which can be achieved by compensating for the aforementioned phase lag. In this context, the present work proposes an innovative compensator based on a notch filter specifically designed for this purpose. Both the filter and the compensator were developed with the objective of expanding the stable operating region of the system, making it less sensitive to variations in the grid impedance or in LCL filter parameters [7]. The compensator design details, including the parameter definitions of the notch filter, will be presented in this section.

Several studies in the literature employ notch filters as an integral part of damping solutions, as exemplified in [11] and [18]. In summary, these works propose techniques to dynamically estimate the resonance frequency of the LCL filter, since it may vary depending on the grid or filter impedance. This estimated parameter is then used to tune the notch filter's rejection band to match the LCL filter's resonance peak, thereby providing damping. In addition to these approaches, several other authors utilize notch filters for the purpose of optimizing the current control loop dynamics [19]–[22]. However, the use of a notch filter for time-delay compensation, as proposed in the present work, has not been previously explored.

The notch filter adopted in this work can be represented as:

$$G_{FN}(s) = \frac{s^2 + \omega_n^2}{s^2 + 2\zeta\omega_n s + \omega_n^2}, \tag{24}$$

where ω_n is the notch frequency, or center rejection frequency, and the parameter ζ is known as the damping factor. The latter controls the damping of the filter, affecting both the width of the rejection band and the phase variation around the rejection frequency. In this way, different values of ζ influence the smoothness of the phase deviation in the filter's frequency response, as can be observed in Fig. 10.

Fig. 10 shows the Bode plot of the discrete-time notch filter, $G_{FN}(z)$, with the parameter ω_n tuned to the Nyquist frequency. This tuning is adopted to prevent the typical phase jump at the Nyquist frequency from affecting the stable region of the current control or amplifying high-frequency noise [23]. The figure also shows the phase deviation of the notch filter relative to the phase of the time delay, represented by $G_{td}(z)$, as the values of ζ vary. It can be observed that the parameter $\zeta = 2.5$ provides the closest phase match between the notch filter and the time delay, which is the critical behavior of interest in this work, since, as previously discussed, the system time delay manifests as a phase lag. Regarding the magnitude response of the filter, it remains at

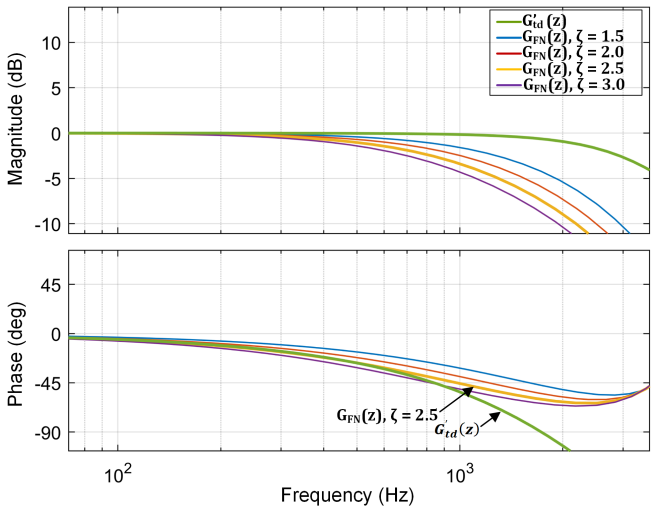

FIGURE 10. Comparison between the frequency responses of the time delay, $G_{td}(z)$, and the notch filter, $G_{FN}(z)$, varying the parameter ζ.

0 dB over a wide frequency range, decaying only beyond 200 Hz. Therefore, given that the frequency of interest is 60 Hz, the magnitude variations occurring above 200 Hz will not affect the results.

Since the main objective is to compensate for the time delay as effectively as possible, it is essential that the compensator introduces a phase lead closely matching the phase lag caused by the delay. One way to achieve this phase lead is by taking the inverse of the notch filter transfer function, after selecting the value of ζ that provides the best phase alignment between the notch filter and the time delay, as previously shown in Fig. 10. The compensator can thus be expressed as

$$G_{cd}(s) = \frac{1}{G_{FN}(s)} = \frac{s^2 + 2\zeta\omega_n s + \omega_n^2}{s^2 + \omega_n^2}. \tag{25}$$

It is important to emphasize that the purpose of using the inverse-notch configuration is not related to magnitude shaping but to achieving a specific phase-lead characteristic that counteracts the delay-induced phase lag. Unlike a conventional phase-lead compensator, whose phase advance is limited and depends on the pole-zero ratio, the inverse-notch structure produces a broader and smoother phase profile that effectively mirrors the delay phase response. When tuned at the Nyquist frequency, the compensator avoids magnitude amplification and phase discontinuities typically associated with notch filters, resulting in a flat magnitude response and a controlled phase behavior suitable for delay compensation.

The Bode plot of the discretized compensator, $G_{cd}(z)$, is shown in Fig. 11. In this figure, the phase lead characteristic of the proposed compensator can be observed, along with the the corresponding total phase lag introduced by $G_{td}(s)$ and the designed notch filter $G_{FN}(z)$. The compensator was discretized using the bilinear (Tustin) transform, chosen because it preserves stability by mapping poles from the left-half s-plane to inside the unit circle in the z-domain,

while avoiding additional phase lag. This property makes the bilinear transform particularly suitable for the proposed compensator, whose performance depends on maintaining the desired phase characteristics that counteract the delay-induced lag.

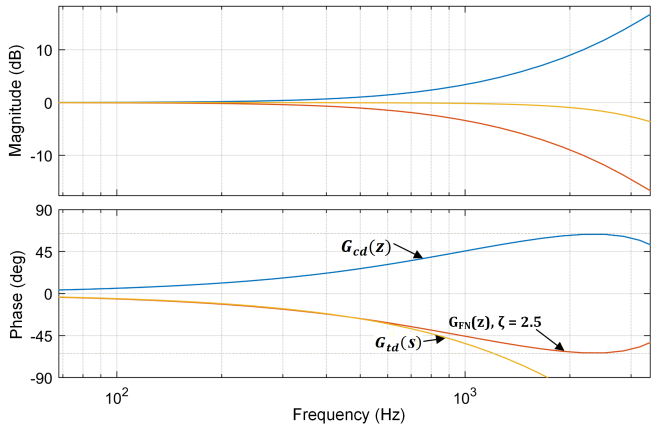

FIGURE 11. Bode plots of the notch filter, $G_{FN}(z)$, in brown; of the time delay, $G_{td}(s) = e^{-1.5T_s s}$, in yellow; and of the proposed compensator, $G_{cd}(z)$, in blue. It is observed that the phase lead of $G_{cd}(z)$ compensates for the phase delay of $G_{td}(z)$.

The block diagram of the system incorporating the proposed compensator is shown in Fig. 12. Fig. 13, in turn, presents the root locus diagram for the compensated system, considering the four resonance frequencies listed in Table 1. This diagram illustrates the trajectories of the resonant poles as a function of the variation of the active damping loop gain. In comparison with the root locus diagram shown in Fig. 7, which refers to the uncompensated system, it can be observed that the poles associated with the frequencies f_{r2}, f_{r3}, and f_{r4} previously followed trajectories outside the unit circle, indicating instability. With the proposed compensator, however, these poles now follow trajectories that cross into the interior of the unit circle. This demonstrates that, with the compensator, poles that were previously unstable have become stable, even for frequencies above $f_s/6$, which is the critical frequency for the uncompensated system.

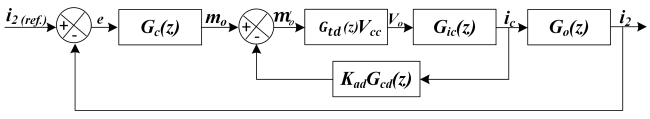

FIGURE 12. Block diagram of the system with the proposed compensator.

A key feature in the diagram shown in Fig. 13 is the pole associated with the highest resonance frequency, f_{r4}, represented in purple. Initially, this pole follows a trajectory inside the unit circle, but it becomes unstable when it crosses the frequency corresponding to $0.282f_s$, or approximately $f_s/3$. Therefore, resonant poles with frequencies higher than $f_s/3$ become unstable, indicating that this is the new critical frequency for the system with the proposed compensator.

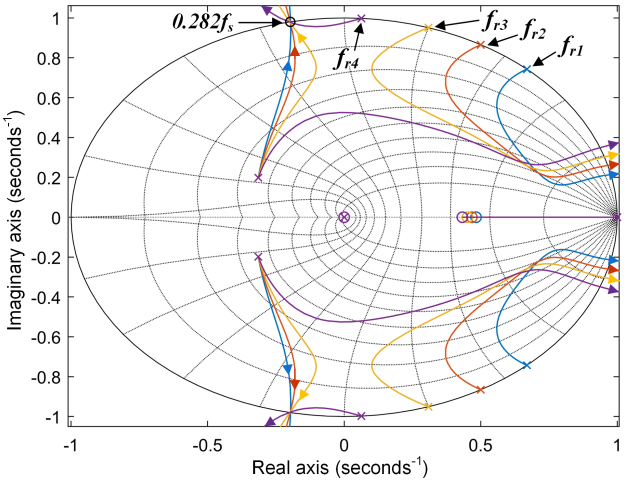

FIGURE 13. Root locus of the system with the proposed time delay compensator demonstrating the increase in the critical frequency, which consequently expands the stable region of the system.

Based on this result, it can be concluded that the proposed compensator has increased the critical frequency f_c from $f_s/6$ to approximately $f_s/3$, thus expanding the system's stability region as intended.

V. EXPERIMENTAL RESULTS

This section presents the experimental results obtained to validate the theoretical analysis discussed earlier and to demonstrate the effectiveness of the proposed notch-filter-based compensator. The experimental setup, illustrated in Fig. 14, consists of a Typhoon HIL-402, which emulates the inverter and the grid as considered in the theoretical analysis, a dSPACE MicroLabBox DS1202, which implements the inverter control system, a Tektronix MSO46 mixed-signal oscilloscope, and a laptop. The tests were carried out under the conditions assumed in the theoretical analysis, using the parameters listed in Table 1.

A. Experimental Verification of Stability Regions

The initial experiments were conducted on the system with active damping (considering the condition $K_{ad} > K_p$) but without the proposed compensator. Two LCL filters with different resonance frequencies were used: $f_{r1} = 1.34\,\text{kHz}$ and $f_{r2} = 1.67\,\text{kHz}$, as listed in Table 1. The first resonance frequency, f_{r1}, is lower than the uncompensated critical frequency f_c, and is intended to demonstrate that the employed active damping effectively stabilizes the uncompensated system for resonance frequencies below f_c. In contrast, when the resonance frequency is set to $f_{r2} = f_c$ the results clearly indicate the loss of stability, confirming that the uncompensated system becomes unstable once the critical frequency is reached. This behavior is presented in Fig. 15, which shows the experimental waveforms of the currents injected to the grid, i_{2abc}, as the resonance frequency is

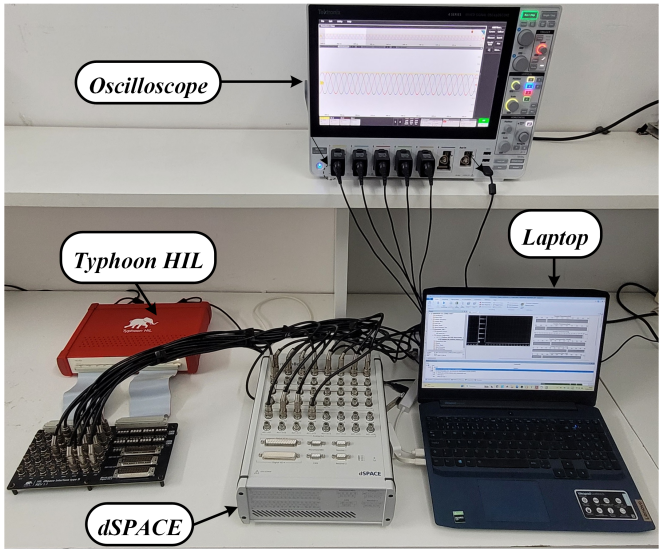

FIGURE 14. Experimental setup.

switched from f_{r1} to f_{r2}. The system remains stable at f_{r1} but becomes unstable at f_{r2}, thus experimentally validating the critical frequency and the theoretical stability predictions for the uncompensated system.

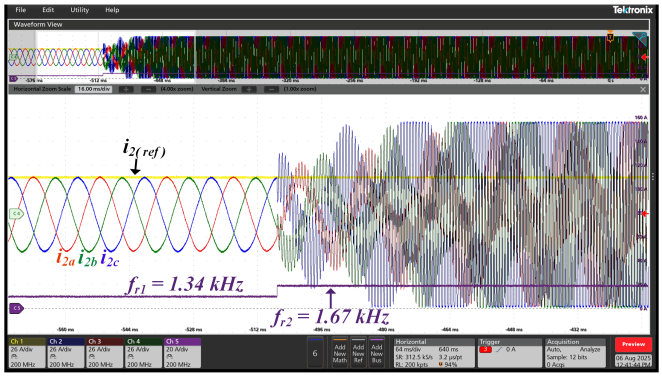

FIGURE 15. Experimental waveforms of the currents injected to the grid when the resonance frequency changes from $f_{r1} < f_c$ to $f_{r2} = f_c$.

Continuing the experiments, the next step evaluates the uncompensated system behavior when the active damping loop gain satisfies $K_{ad} < K_p$. Theoretically, this condition eliminates active damping, making the system behave as undamped. Thus, the system is stable for resonance frequencies above the critical frequency, $f_{res} > f_c$, and unstable below it, $f_{res} < f_c$. Fig. 16 experimentally confirms this prediction by showing the waveforms of currents injected to the grid with the active damping gain set to $K_{ad} < K_p$. The system remains stable at $f_{r3} > f_c$, but becomes unstable when the resonance frequency decreases to $f_{r1} < f_c$. This clearly delineates the stability regions of the undamped system, in line with prior theoretical analysis.

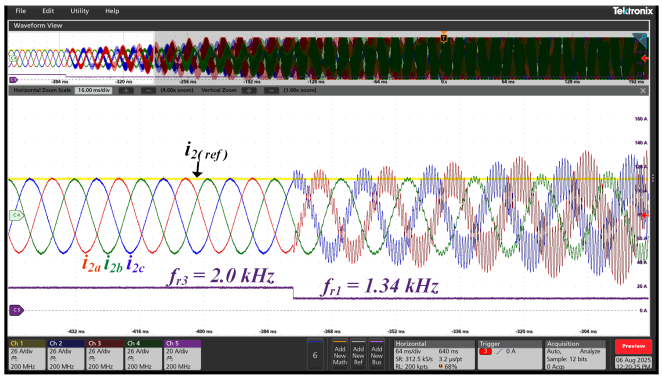

FIGURE 16. Experimental waveforms of the currents injected to the grid when the resonance frequency changes from $f_{r3} > f_c$ to $f_{r1} < f_c$ with $K_{ad} < K_p$, demonstrating the loss of active damping due to K_{ad}.

B. Experimental Verification of K_{ad} Constraints

As theoretically predicted in Section III and confirmed by the previous experimental results, the condition $K_{ad} > K_p$ is essential for maintaining the effectiveness of the active damping loop. In addition, the theoretical analysis establishes that K_{ad} must remain within specific bounds to guarantee system stability, defining $K_{ad(min)}$ and $K_{ad(max)}$ as the lower and upper limits, respectively. To experimentally validate these limits, Fig. 17 illustrates the system response for $K_{ad} = K_{ad(min)}$ and $f_{res} = f_{r1}$ under a step change in the current reference, where an overshoot of 16.1 % and a THD of 1.47 % are observed.

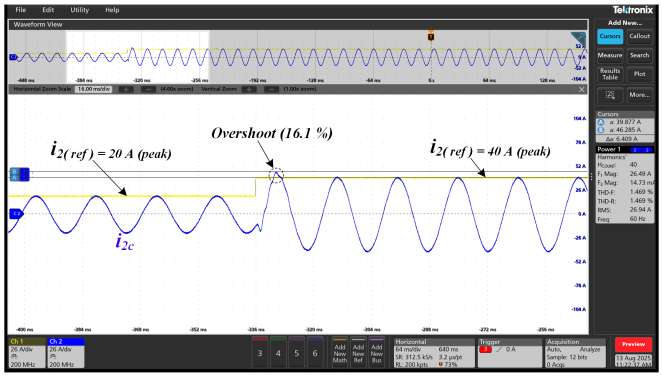

FIGURE 17. Experimental grid current waveform for $K_{ad} = K_{ad(min)}$ and $f_{res} = f_{r1}$, under a step change in current reference. Overshoot: 16.1 %, THD: 1.47 %.

On the other hand, Fig. 18 shows the same waveform, with the only change being the active damping gain set to $K_{ad} = 0.045$ — the midpoint between $K_{ad(min)}$ and $K_{ad(max)}$. A degradation in waveform quality is observed compared to the previous case, now exhibiting a THD of 2.5 % and an overshoot of 31.9 %.

Finally, adopting the theoretical value $K_{ad} = K_{ad(max)}$, the current waveform exhibits higher harmonic distortion and overshoot values compared to the previous cases, as shown in Fig. 19, which presents a THD of 3.75 % and an overshoot

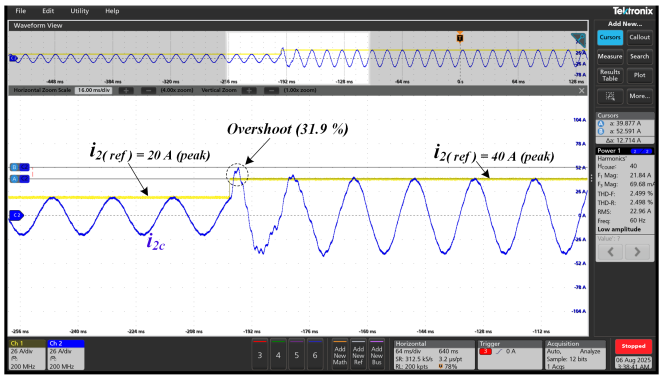

FIGURE 18. Experimental grid current waveform for $K_{ad} = K_{ad(avg)} = 0.045$ and $f_{res} = f_{r1}$, under a step change in current reference. Overshoot: 31.9 %, THD: 2.5 %.

of 35.6 %. It is important to note that with the gain set to $K_{ad(max)}$, the system behavior becomes significantly more oscillatory, approaching instability.

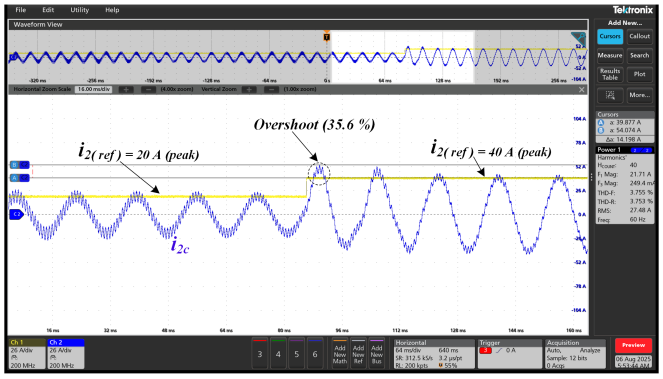

FIGURE 19. Experimental grid current waveform for $K_{ad} = K_{ad(max)}$ and $f_{res} = f_{r1}$, under a step change in current reference. Overshoot: 35.6 %, THD: 3.75 %.

Figs. 17 to 19 show that increasing the gain K_{ad} progressively deteriorates the system's dynamic performance, resulting in larger overshoot, higher harmonic distortion, and a tendency toward instability. This behavior is consistent with the theoretical prediction from Section III, which associates higher K_{ad} values with a reduction in the system's phase margin—an effect that, in practice, manifests precisely as the degraded transient behavior observed in these figures.

C. Experimental Validation of the Proposed Compensator

To assess the effectiveness of the proposed controller, the following results present the system behavior with its implementation, enabling a direct comparison with the previous uncompensated case. Accordingly, Fig. 20 depicts the experimental grid current waveform under the same operating conditions as in Fig. 17, but now with the proposed controller enabled. A marked improvement in the system's dynamic performance is observed, with the overshoot reduced from 16.1 % to 10.5 % and the THD from 1.47 % to 1.09 %, compared to the uncompensated case in Fig. 17.

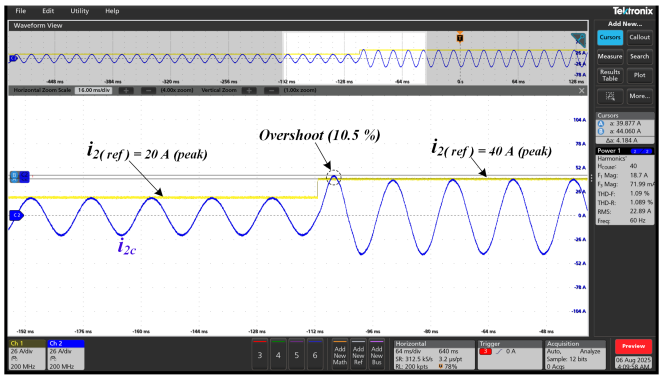

FIGURE 20. Experimental grid current waveform for $K_{ad} = K_{ad(min)}$ and $f_{res} = f_{r1}$ under a step change in current reference, with the proposed compensator. Overshoot: 10.5 %; THD: 1.01 %.

The improvement in the dynamic response observed in the latter result is a direct consequence of the expanded stability region provided by the proposed compensator. This expansion can be verified in Figure 21, which shows that the system remains stable even when the resonant frequency shifts from f_{r1} to $f_{r2} = f_c$. As shown in Figure 15, under the same conditions, the system without the proposed compensator became unstable for $f_{r2} = f_c$.

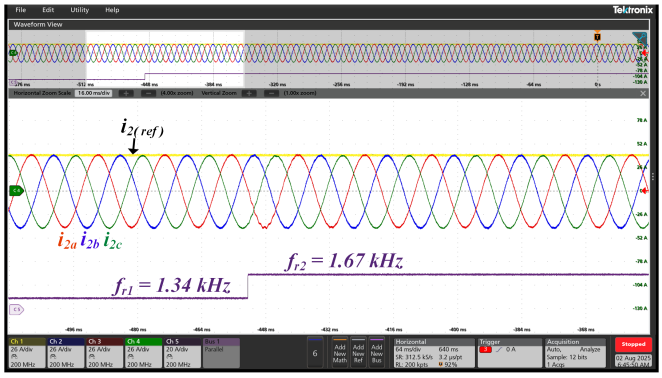

FIGURE 21. Experimental grid current waveform with the proposed compensator when the resonance frequency shifts from $f_{r1} < f_c$ to $f_{r2} = f_c$, demonstrating stable operation at both frequencies.

Figure 22, in turn, demonstrates that the system remains stable even when the resonance frequency surpasses the critical frequency. In this case, the resonance frequency increases from f_{r1} to f_{r4}, which is approximately 45 % higher than f_c. Nevertheless, the system maintains stability, indicating that the critical frequency of the compensated system is higher than f_{r4}.

Finally, when the resonance frequency is increased to $f_{res} = 2.8$ kHz ($f_{r4} + 0.4$ kHz), the system becomes unstable, as illustrated in Fig. 23. This result confirms that the proposed compensator effectively extends the system's critical frequency. With the compensator in place, the new

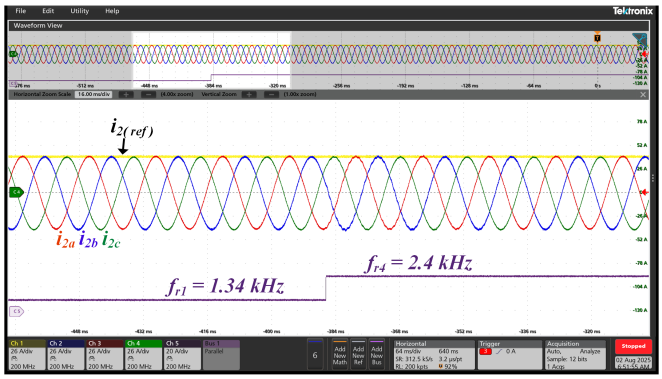

FIGURE 22. Experimental grid current waveform with the proposed compensator when the resonance frequency shifts from $f_{r1} < f_c$ to $f_{r4} = f_c$, demonstrating stable operation at both frequencies.

critical frequency is established at 2.8 kHz, ensuring stable operation for all resonance frequencies below this threshold.

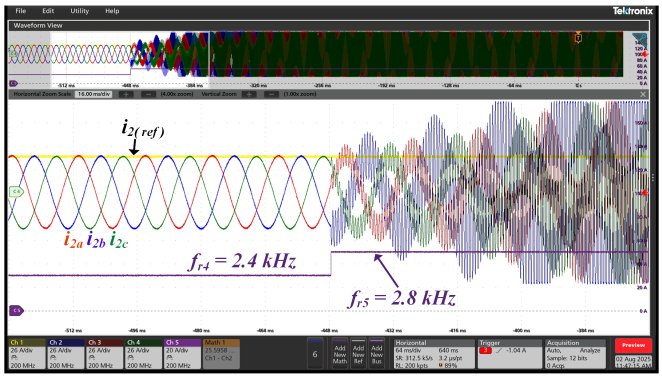

FIGURE 23. Experimental grid current waveform with the proposed compensator as the resonance frequency increases from f_{r4} to $f_{r4} + 0.4$ kHz, illustrating the stability boundary.

VI. CONCLUSION

This paper presented a comprehensive strategy to enhance the stability of LCL-filtered grid-connected inverters. A detailed analysis of the active damping gain (K_{ad}) revealed its critical impact on the system's phase margin, establishing clear design guidelines for its selection to prevent performance degradation—an aspect often overlooked in the literature. The core of this work is a novel notch-filter-based compensator that directly counteracts system delays, successfully shifting the critical frequency from $f_s/6$ to approximately $f_s/3$ and thus expanding the stable operating region without computational overhead. Theoretical analyses and experimental validations on a hardware-in-the-loop (HIL) confirmed the proposed methodology's effectiveness, demonstrating superior transient response, reduced harmonic distortion and robust stability, making it a promising solution for robust grid-connected inverter applications.

ACKNOWLEDGMENTS

The author acknowledges the Brazilian National Council for Scientific and Technological Development (CNPq) for funding this paper through project no. 406722/2022-6

AUTHOR'S CONTRIBUTIONS

J.N.D.SILVA: Conceptualization, Data Curation, Formal Analysis, Investigation, Methodology, Validation, Writing – Original Draft. **F.A.D.C.BAHIA:** Conceptualization, Data Curation, Formal Analysis, Methodology, Visualization. **A.P.N.TAHIM:** Conceptualization, Formal Analysis, Investigation, Software. **D.A.FERNANDES:** Formal Analysis, Funding Acquisition, Investigation, Methodology. **F.F.COSTA:** Conceptualization, Investigation, Methodology, Project Administration, Resources, Supervision.

PLAGIARISM POLICY

This article was submitted to the similarity system provided by Crossref and powered by iThenticate – Similarity Check.

DATA AVAILABILITY

The data used in this research is available in the body of the document.

REFERENCES

[1] R. Teodorescu, F. Blaabjerg, M. Liserre, A. Dell'Aquila, "A stable three-phase LCL-filter based active rectifier without damping", *in 38th IAS Annual Meeting on Conference Record of the Industry Applications Conference, 2003.*, vol. 3, pp. 1552–1557 vol.3, 2003, doi:10.1109/IAS.2003.1257762.

[2] J. Dannehl, C. Wessels, F. W. Fuchs, "Limitations of Voltage-Oriented PI Current Control of Grid-Connected PWM Rectifiers With LCL Filters", *IEEE Transactions on Industrial Electronics*, vol. 56, no. 2, pp. 380–388, 2009, doi:10.1109/TIE.2008.2008774.

[3] S. G. Parker, B. P. McGrath, D. G. Holmes, "Regions of Active Damping Control for LCL Filters", *IEEE Transactions on Industry Applications*, vol. 50, no. 1, pp. 424–432, 2014, doi:10.1109/TIA.2013.2266892.

[4] J. Wu, X. Jia, Y. Cui, D. Xu, "Grid-Connected Current-Delayed Cascade Feedback Control Strategy for LCL Inverters", *in 2024 IEEE 7th International Electrical and Energy Conference (CIEEC)*, pp. 315–320, 2024, doi:10.1109/CIEEC60922.2024.10583223.

[5] R. R. Kar, R. Wandhare, "Enhanced Stability and Control of Voltage Source Converters With LCL Filter in Weak Grid", *IEEE Journal of Emerging and Selected Topics in Industrial Electronics*, vol. 6, no. 1, pp. 271–283, 2025, doi:10.1109/JESTIE.2024.3427363.

[6] Z. Xin, X. Wang, P. C. Loh, F. Blaabjerg, "Grid-Current-Feedback Control for LCL-Filtered Grid Converters With Enhanced Stability", *IEEE Transactions on Power Electronics*, vol. 32, no. 4, pp. 3216–3228, 2017, doi:10.1109/TPEL.2016.2580543.

[7] S. Bibian, H. Jin, "Time delay compensation of digital control for DC switchmode power supplies using prediction techniques", *IEEE Transactions on Power Electronics*, vol. 15, no. 5, pp. 835–842, 2000, doi:10.1109/63.867672.

[8] R. Raj Kar, R. Wandhare, "Passivity Principle-Based Active Damper Design to Enhance Stability of a Voltage Source Converter for Weak Grid Scenario", *IEEE Journal of Emerging and Selected Topics in Power Electronics*, vol. 12, no. 5, pp. 5076–5089, 2024, doi:10.1109/JESTPE.2024.3406566.

[9] D. Pan, X. Ruan, C. Bao, W. Li, X. Wang, "Capacitor-Current-Feedback Active Damping With Reduced Computation Delay for Improving Robustness of LCL-Type Grid-Connected Inverter", *IEEE Transactions on Power Electronics*, vol. 29, no. 7, pp. 3414–3427, 2014, doi:10.1109/TPEL.2013.2279206.

[10] X. Li, X. Wu, Y. Geng, X. Yuan, C. Xia, X. Zhang, "Wide Damping Region for LCL-Type Grid-Connected Inverter With an Improved Capacitor-Current-Feedback Method", *IEEE Transactions on Power Electronics*, vol. 30, no. 9, pp. 5247–5259, 2015, doi:10.1109/TPEL.2014.2364897.

[11] R. Peña-Alzola, M. Liserre, F. Blaabjerg, M. Ordonez, T. Kerekes, "A Self-commissioning Notch Filter for Active Damping in a Three-Phase LCL -Filter-Based Grid-Tie Converter", *IEEE Transactions on Power Electronics*, vol. 29, no. 12, pp. 6754–6761, 2014, doi:10.1109/TPEL.2014.2304468.

[12] J. Ma, X. Wang, F. Blaabjerg, L. Harnefors, W. Song, "Accuracy Analysis of the Zero-Order Hold Model for Digital Pulse Width Modulation", *IEEE Transactions on Power Electronics*, vol. 33, no. 12, pp. 10826–10834, 2018, doi:10.1109/TPEL.2018.2799819.

[13] B. Lathi, *Linear Systems and Signals, 2nd edition*, Oxford University Press, 2004.

[14] A. G. Yepes, F. D. Freijedo, J. Doval-Gandoy, López, J. Malvar, P. Fernandez-Comesaña, "Effects of Discretization Methods on the Performance of Resonant Controllers", *IEEE Transactions on Power Electronics*, vol. 25, no. 7, pp. 1692–1712, 2010, doi:10.1109/TPEL.2010.2041256.

[15] D. Zmood, D. Holmes, "Stationary frame current regulation of PWM inverters with zero steady-state error", *IEEE Transactions on Power Electronics*, vol. 18, no. 3, pp. 814–822, 2003, doi:10.1109/TPEL.2003.810852.

[16] M. Liserre, F. Blaabjerg, S. Hansen, "Design and control of an LCL-filter-based three-phase active rectifier", *IEEE Transactions on Industry Applications*, vol. 41, no. 5, pp. 1281–1291, 2005, doi:10.1109/TIA.2005.853373.

[17] M. B. Saïd-Romdhane, M. Naouar, I. S. Belkhodja, E. Monmasson, "Simple and systematic LCL filter design for three-phase grid-connected power converters", *Mathematics and Computers in Simulation*, vol. 130, pp. 181–193, 2016, doi:10.1016/j.matcom.2015.09.011.

[18] M. Liserre, A. Dell'Aquila, F. Blaabjerg, "Genetic algorithm-based design of the active damping for an LCL-filter three-phase active rectifier", *IEEE Transactions on Power Electronics*, vol. 19, no. 1, pp. 76–86, 2004, doi:10.1109/TPEL.2003.820540.

[19] C. Liu, X. Zhang, L. Tan, F. Liu, "A novel control strategy of LCL-VSC based on notch concept", *in The 2nd International Symposium on Power Electronics for Distributed Generation Systems*, pp. 343–346, 2010, doi:10.1109/PEDG.2010.5545767.

[20] Q. Zhao, F. Liang, W. Li, "A new control scheme for LCL-type grid-connected inverter with a Notch filter", *in The 27th Chinese Control and Decision Conference (2015 CCDC)*, pp. 4073–4077, 2015, doi:10.1109/CCDC.2015.7162637.

[21] L. Zhou, M. Preindl, "Optimal Tracking and Resonance Damping Design of Cascaded Modular Model Predictive Control for a Common-Mode Stabilized Grid-Tied $LC\dot{L}$ Inverter", *IEEE Transactions on Power Electronics*, vol. 37, no. 8, pp. 9226–9240, 2022, doi:10.1109/TPEL.2022.3159599.

[22] Y. Jing, A. A. Durra, E. F. El-Saadany, "An Adaptive Digital Notch Filter Based on Grid Impedance Estimation for Improving LCL Filter Peformance", *in 2018 IEEE/PES Transmission and Distribution Conference and Exposition (TD)*, pp. 1–5, 2018, doi:10.1109/TDC.2018.8440296.

[23] Z. Xin, X. Wang, P. C. Loh, F. Blaabjerg, "Realization of Digital Differentiator Using Generalized Integrator For Power Converters", *IEEE Transactions on Power Electronics*, vol. 30, no. 12, pp. 6520–6523, 2015, doi:10.1109/TPEL.2015.2442414.

BIOGRAPHIES

James Neves da Silva holds a B.Sc. in Electrical Engineering from the Federal University of the São Francisco Valley (UNIVASF, 2014) and an M.Sc. from the Federal University of Bahia (UFBA, 2019), where he is currently pursuing a Ph.D. His research focuses on the control and stability of grid-connected converters, particularly methods to expand the stability region of LCL inverters.

Filipe Antônio da Costa Bahia holds a Bachelor's degree in Electrical Engineering (2013) from the Federal University of Paraíba (UFPB). He earned his Master's (2015) and Doctorate (2019) degrees in Electrical Engineering from the Federal University of Campina Grande (UFCG). He is currently an Adjunct Professor at the Department of Electrical and Computer Engineering (DEEC) at the Federal University of Bahia (UFBA). His research interests include power electronic converters, renewable energy generation systems, energy storage systems, electric machine drive systems, and pulse-width modulation (PWM) strategies.

André Pires Nóbrega Tahim holds a Bachelor's degree in Electrical Engineering from the Federal University of Bahia (2004). He earned his Master's degree in Electrical Engineering and Doctorate in Automation and Systems Engineering from the Federal University of Santa Catarina (2009 and 2015, respectively). Since 2015, he has been a faculty member of the Electrical Engineering Department at the Federal University of Bahia (Brazil). His current research interests include modeling and control of energy conversion systems, dynamic systems analysis, DC distribution systems, and power electronics for renewable energy sources.

Darlan Alexandria Fernandes received the B.S. degree in electrical engineering from the Federal University of Paraiba, Brazil, in 2002, and the M.S. and Ph.D. degrees in electrical engineering from the Federal University of Campina Grande, Brazil, in 2004 and 2008, respectively. He was a Visiting Scholar at the Center for Power Electronics Systems (CPES) at the Virginia Polytechnic Institute and State University (Virginia Tech), Blacksburg, United States, from 2018 to 2019. From 2007 to 2011, he was a Professor with the Industry Department in the Federal Center of Technological Education of Rio Grande do Norte. He is currently an Associate Professor with the Department of Electrical Engineering, Federal University of Paraiba, Brazil. His research interests are in the applications of power electronics in distribution systems, power quality, photovoltaic systems, and impedance-based control design techniques for static converters. He is a member of the Brazilian Power Electronics Association (SOBRAEP) and IEEE.

Fabiano Fragoso Costa received his Bachelor's, Master's, and Doctorate degrees in Electrical Engineering from the University of São Paulo, Federal University of Paraíba, and Federal University of Campina Grande in 1997, 2001, and 2005, respectively. He is an Associate Professor in the Department of Electrical Engineering at the Federal University of Bahia. His research interests include the stability and modeling of power converters. He is a full member of the Brazilian Power Electronics Society (SOBRAEP) and a Senior Member of IEEE.